



Accurate Effective Stress Measures: Predicting Creep Life for 3D Stresses Using 2D and 1D Creep Rupture Simulations and Data

Andrea Rovinelli¹ · Mark C. Messner¹ · David M. Parks² · Ting-Leung Sham³

Received: 7 June 2021 / Accepted: 16 August 2021 / Published online: 9 November 2021
© The Minerals, Metals & Materials Society 2021

Abstract

Operating structural components experience complex loading conditions resulting in 3D stress states. Current design practice estimates multiaxial creep rupture life by mapping a general state of stress to a uniaxial creep rupture correlation using effective stress measures. The data supporting the development of effective stress measures are nearly always only uniaxial and biaxial, as 3D creep rupture tests are not widely available. This limitation means current effective stress measures must extrapolate from 2D to 3D stress states, potentially introducing extrapolation error. In this work, we use a physics-based, crystal plasticity finite element model to simulate uniaxial, biaxial, and triaxial creep rupture. We use the virtual dataset to assess the accuracy of current and novel effective stress measures in extrapolating from 2D to 3D stresses and also explore how the predictive accuracy of the effective stress measures might change if experimental 3D rupture data was available. We confirm these conclusions, based on simulation data, against multiaxial creep rupture experimental data for several materials, drawn from the literature. The results of the virtual experiments show that calibrating effective stress measures using triaxial test data would significantly improve accuracy and that some effective stress measures are more accurate than others, particularly for highly triaxial stress states. Results obtained using experimental data confirm the numerical findings and suggest that a unified effective stress measure should include an explicit dependence on the first stress invariant, the maximum tensile principal stress, and the von Mises stress.

Keywords Creep · Crystal plasticity · Effective stress · Multiaxial creep · Triaxial stress

Introduction

High-temperature engineering components operate under general, triaxial, 3D stress states.¹ Even conventional pressure vessels have regions like nozzles where the stress state is not biaxial, and new types of high temperature

components, like compact heat exchangers [1] and metallic core-block in heat-pipe reactors [2], tend to result in complex, triaxial stress distributions. For high-temperature applications, creep-rupture is one of the dominant failure mechanisms and accurate, efficient design requires a method for predicting creep failure for general, multiaxial stress histories.

While components operate under general states of stress, creep experiments are widely available only for uniaxial and biaxial stresses. The most widely used biaxial creep test techniques are tension–torsion tests [3–5] and pressurized tubes [6, 7], often loaded with a combination of pressure and uniaxial tension or compression. Creep experiments for triaxial stress states are possible [8, 9], but the equipment cost, the time required to perform the experiments, and the uncertainty in the stress experienced by the core of the specimen prevent their wide adoption. Without triaxial creep rupture data, engineers and designers can only estimate the creep

✉ Andrea Rovinelli
arovinelli@anl.gov

Mark C. Messner
messner@anl.gov

David M. Parks
dmparks@mit.edu

Ting-Leung Sham
TingLeung.Sham@inl.gov

¹ Applied Materials Division, Argonne National Laboratory, Lemont, USA

² Massachusetts Institute of Technology, Cambridge, USA

³ Idaho National Laboratory, Idaho Falls, USA

¹ Henceforth, we refer to a triaxial stress state as any stress tensor with all three principal values with non-negligible magnitudes.

rupture life, t_r , for triaxial stress states by extrapolating from uniaxial and biaxial experimental data. This extrapolation raises concerns about the accuracy of the predicted rupture times, especially for critical components.

The currently accepted engineering approach correlates the uniaxial tensile creep rupture stress with a time–temperature parameter, such as the one proposed by Larson and Miller [10]. In general, time–temperature parameters have material-dependent coefficients calibrated against uniaxial creep rupture data. Applying this common design approach to a generic complex, stress state, σ , requires a map from the general state of stress to a positive scalar stress value. Any linear or nonlinear map between a generic stress state and a positive scalar equivalent stress is an *effective stress*, σ_{eff} . The goal in developing an effective stress measure is to find a map such that the creep rupture times from multi-axial and uniaxial loadings (e.g., in a creep rupture test) are the same if the scalar stress measures from the two loading states are the same. Often effective stress models have material-dependent coefficients calibrated using multi-axial creep rupture data. For isotropic materials, a generic stress tensor can be described using only three independent values, such as the *ordered* principal stresses, i.e., $\sigma_I \geq \sigma_{II} \geq \sigma_{III}$, or, equivalently, stress invariants.

The first effective stresses were developed in the context of plasticity as yield criteria for multi-axial loading conditions. In 1864, Tresca [11] proposed an effective stress measure, σ_{Tresca} , based on the maximum shear theory. In 1913, von Mises [12] noticed that a yield surface based upon σ_{Tresca} exhibits singularities and proposed a new measure, σ_{VM} , based on the maximum distortional energy. Being developed for classical plasticity, both the Tresca and the von Mises stresses neglect the influence of the hydrostatic stress and they cannot discriminate between tension and compression. More importantly, for a pure hydrostatic loading conditions $\sigma_{\text{VM}} = \sigma_{\text{Tresca}} = 0$. Nevertheless, both measures are used as creep effective stresses.

Sdobyrev introduced the idea of creep-specific effective stress measures with material-dependent parameters. He noted the creep rupture life of pure copper correlates well with the maximum tensile principal stress ($\langle \sigma_I \rangle$), the life of aluminum correlates well with the von Mises stress, and the creep life of some high-temperature structural alloys falls between these extremes. Here, the angled brackets, i.e., $\langle x \rangle$, are the Macaulay brackets. Given this evidence, Sdobyrev proposed an effective stress, σ_{Sd} , defined as a linear combination of the von Mises stress and maximum tensile principal stress.

Hayhurst and co-workers [13–16] pointed out that the measure proposed by Sdobyrev does not accurately predict the creep rupture life of materials that are sensitive to the hydrostatic stress. Therefore, they proposed a different measure, σ_{HLM} , which expands the Sdobyrev definition by

including the absolute value of the first stress invariant, i.e., $I_1 = \sigma_I + \sigma_{II} + \sigma_{III}$. Neglecting the sign of the first stress invariant is an unusual choice for creep applications because it implies a negative hydrostatic stress promotes creep damage. However, Hayhurst and co-workers focused on pressurized thin-walled structures and therefore compression was not expected.

Huddleston used a different approach and proposed a measure, σ_{Hudd} , that can discern between the effect of positive and negative hydrostatic stress [17]. Huddleston used an exponential function including the first stress invariant to scale the von Mises stress and demonstrated that σ_{Hudd} is 2–5 times more accurate than the Tresca and von Mises measures [18, 19] when predicting the rupture time of biaxial creep experiment results. However, Huddleston’s model does not explicitly account for the effect of the maximum tensile principal stress, which was deemed crucial for some materials by his predecessors. Several high-temperature design codes, such as Section III, Division 5 of the ASME Boiler and Pressure Vessel Code [20], the fitness-for-service manual FFS-1 [21] and the British R5 [22], adopt the Huddleston stress.

Other effective stress measures are currently used in the literature and by other high temperature design codes. For instance, the French high-temperature nuclear code, RCC-MRx [23], allows the use of two different measures, both including the effect of the first stress invariant. The first measure, $\sigma_{\text{RCC}_{\text{VM}}}$, is a linear combination of the von Mises stress and the first stress invariant. The other measure, $\sigma_{\text{RCC}_{\text{Tresca}}}$, is similar to the first but includes σ_{Tresca} instead of the von Mises stress. The variety of equivalent stress measures used in the literature and for design purposes raises the question of which measure is more accurate and if there is any measure that is accurate for all materials. To the knowledge of the authors, no comprehensive review comparing the accuracy of different stress measures for multiple materials exists.

Physics-based, micromechanical models, including the dominant damage mechanisms, can be used to extrapolate a material response to loading conditions for which experimental data are not readily available. Creep rupture is the final effect of grain boundary cavitation, which is caused by the accumulation of points and line defect at preferably oriented grain boundaries. Messner et al. [24] were first to present a *three-dimensional* crystal plasticity finite element framework including grain boundary cavitation and grain boundary sliding. This paper employs such a model to examine creep rupture under arbitrary, 3D states of stress for Grade 91, which is a ferritic-martensitic steel.

This work has three goals: (i) assess the accuracy of effective stress measures calibrated against biaxial creep data when used to estimate the creep rupture life for tri-axial stress states, (ii) assess if the availability of tri-axial creep rupture data would improve creep life predictions, and

(iii) assess if any of the investigated stress measures can be considered universally accurate for all stress states and materials. For the first and second goals, we use the results of crystal plasticity finite-element simulations for Grade 91 to construct a complete data set of synthetic creep rupture data for uniaxial, biaxial and triaxial stress states. We use synthetic uniaxial creep rupture data to construct a piecewise log-linear uniaxial creep rupture correlation. Then, we calibrate each effective stress measure's material-specific parameters, if any, using only synthetic biaxial results and evaluate their accuracy as creep-rupture predictors by computing the relative mean square error against the synthetic creep rupture time for triaxial stress states. This approach mimics the current engineering approach and assesses the feasibility of extrapolating from biaxial rupture data. Also, to gain further insights into the extrapolation ability of each metric, we investigated the relationship between the signed relative error and the triaxiality factor. To assess the importance of performing triaxial creep tests, we then include synthetic triaxial rupture data in the calibration set and reassess the accuracy of each effective stress measure. Finally, we use available biaxial experimental rupture data from the literature to evaluate the different stress measures against experimental data and determine if the measures found to be the most accurate against the simulation results for Grade 91 remain accurate when applied to other materials, using actual biaxial rupture measurements.

Methodologies

Constitutive Models

The grain model and the grain boundary cavitation model used in this work are the one proposed in [24]. In this section, we present the equations and describe the key features of the model. The model parameters used in this work were calibrated to describe the behavior of Grade 91 at 600 °C. For a more detailed discussion, refer to [24].

The Grain Model

Experimental results from [25, 26] exhibit a sudden change in slope of the minimum creep rate as a function of stress. In both studies, the authors related the change in slope to a switch between two different creep deformation mechanism. At low stress levels, the stress exponent of Grade 91 is almost unity, thus suggesting the main deformation mechanism is the diffusion of point defects. At high stress levels, dislocation

Table 1 Grain bulk material parameters for Grade 91 at 600 °C

Symbol	Description	Value	Units
E	Young's modulus	150×10^3	MPa
ν	Poisson's ratio	0.285	Unitless
n	Voce hardening exponent	12	Unitless
τ_0	Initial slip resistance	40	MPa
τ_{sat}	Saturation slip resistance	12	MPa
θ_0	Slip hardening constant	66.67	MPa h ⁻¹
$\dot{\gamma}_0$	Prefactor	9.55×10^{-8}	Unitless
A	Diffusional creep constant	1.2×10^{-9}	MPa ⁻¹ h ⁻¹

creep becomes predominant, and stress exponent increases approximately to 12. Both mechanisms are active within the grains at the same time and contribute to the measured creep strain; hence, in the numerical model both mechanism must contribute to the rate of deformation tensor:

$$D = D_{diff} + D_{disl} \quad (1)$$

The grain model uses a linear stress-based relationship to incorporate the effect of diffusion creep:

$$D_{diff} = As \quad (2)$$

where s is the deviatoric part of the Cauchy stress and A is the self-diffusion coefficient.

Dislocations glide and climb on preferred crystallographic planes and directions. The model incorporates dislocation creep within a grain using crystal plasticity, and includes the apparent hardening behavior exhibited by Grade 91 using an isotropic Voce hardening model:

$$D_{disl} = \sum_{r=1}^{N_{ss}} \dot{\gamma}^r \text{sym}(m^r \otimes n^r) \quad (3)$$

$$\dot{\gamma}^r = \dot{\gamma}_0 \left(\frac{\tau^r}{\tau_0 + \tau_w} \right)^n \quad (4)$$

$$\dot{\tau}_w = \theta_0 \left(1 - \frac{\tau_w}{\tau_{sat}} \right) \sum_{r=1}^{N_{ss}} |\dot{\gamma}^r| \quad (5)$$

where r is the slip system index, n^r is a slip system unit normal, m^r is a slip system unit direction vector, τ^r is the resolved shear stress, $\dot{\gamma}^r$ the slip system shear rate, τ_w is the work hardening contribution to the slip resistance, and N_{ss} is the number of slip systems. In this work, we consider only the 12 slip systems belonging to the $\langle 111 \rangle \{ 110 \}$ family.

Table 1 presents the coefficients for the grain model used in the simulations.

Grain Boundary Cavitation Model

The grain boundary cavitation model presented here extends the model proposed by Messner et al. [24] from purely viscous to visco-elastic, using a Maxwell model [2]. The grain boundary model stems from the work of Sham and Needleman [27, 28] on the effect of mass transport and stress triaxiality on grain boundary void growth. Van der Giessen and co-workers extended the Sham and Needleman model to higher triaxiality values [29, 30] and proposed a continuous cavity nucleation model based on stress and accumulated creep strain [31]. Messner et al. also extended the grain boundary sliding model proposed by Ashby and colleagues [32–34] to include the effect of grain boundary sliding on creep damage.

Grain boundary opening is related to the average cavity size and spacing. The cavity growth rate, \dot{a} , is described in terms of cavity volume rate, \dot{V} , which has two terms: the first term, \dot{V}^D , accounts for the effect of the opening traction and the grain boundary diffusivity, and the second term, \dot{V}^{triax} , accounts for the effect of stress triaxiality and the accumulated creep strain experienced by the material in proximity of the grain boundary. In this work, we define the triaxiality factor as:

$$T_f = \frac{I_1}{\sigma_{VM}} \tag{6}$$

With this definition, $T_f = 1$ for tensile uniaxial loading conditions. The grain boundary porosity, which is the square of the ratio between the cavity size, a , and the cavity spacing b , represents the damaged grain boundary area fraction. The cavity nucleation model describes the cavity spacing evolution, \dot{b} , as function of the opening traction T_N and local creep deformation rate. Cavity nucleation begins only after the neighboring grains have accumulated sufficient plastic strain. Equations 7–18 fully define the grain boundary cavitation model, and Table 2 contains the calibrated parameter values and their descriptions.

$$\dot{a} = \frac{\dot{V}}{4\pi h(\Psi)a^2} \tag{7}$$

$$\dot{b} = \begin{cases} -\pi b^3 F_N \left(\frac{\langle T_N \rangle}{\Sigma_0}\right)^\beta \dot{\epsilon}_{eq}^C & \text{after } \left(\frac{\langle T_N \rangle}{\Sigma_0}\right)^\beta \int_0^t |\dot{\epsilon}_{eq}^C| dt \geq \frac{N_I}{F_N} \\ 0 & \text{otherwise} \end{cases} \tag{8}$$

$$\dot{T}_N = \left(\llbracket \dot{u} \rrbracket_N - \frac{\dot{V}(T_N)}{\pi b^2} \right) \frac{w}{E_{GB} \frac{a}{b}} \tag{9}$$

$$\dot{T}_{S_{1/2}} = \left(\llbracket \dot{u} \rrbracket_{S_{1/2}} - \frac{T_{S_{1/2}}}{\eta_{GB} f_S} \right) \frac{w}{G_{GB} \frac{a}{b}}$$

Table 2 Grain boundary cavitation material parameters for Grade 91 at 600 °C

Symbol	Description	Value	Units
β	Traction nucleation exponent	2	Unitless
n_{GB}	Creep rate exponent	5	Unitless
a_0	Initial cavities half radius	5×10^{-5}	mm
b_0	Initial cavities half spacing	0.06	mm
D	Grain boundary diffusion coefficient	1×10^{-15}	$\text{mm}^3 \text{MPa}^{-1} \text{h}^{-1}$
Ψ	Cavity half tip angle	75	°
Σ_0	Traction normalization parameter	200	MPa
$\frac{F_N}{N_I}$	Normalized nucleation rate constant	2×10^4	Unitless
$\frac{N_{max}}{N_I}$	Normalized maximum cavity density	1×10^3	Unitless
E_{GB}	Interface Young modulus	150×10^3	MPa
G_{GB}	Interface in-plane Shear modulus	58.63×10^3	MPa
η_{GB}	Sliding viscosity	1×10^6	MPa h mm^{-1}

$$\dot{V} = \dot{V}^D + \dot{V}^{triax} \tag{10}$$

$$\dot{V}^D = 8\pi D \frac{T_N}{q(f)} \tag{11}$$

$$\dot{V}^{triax} = \begin{cases} 2\dot{\epsilon}_{eq}^C a^3 \pi h(\Psi) m \left\{ \alpha_n \left| \frac{T_f}{3} \right| + \beta_n(m) \right\}^n & \text{if } \left| \frac{T_f}{3} \right| \geq 1 \\ 2\dot{\epsilon}_{eq}^C a^3 \pi h(\Psi) \left\{ \alpha_n + \beta_n(m) \right\}^n \frac{T_f}{3} & \text{if } \left| \frac{T_f}{3} \right| < 1 \end{cases} \tag{12}$$

with $\tag{13}$

$$f = \max \left(\frac{a^2}{(a + 1.5L)^2}, \frac{a^2}{b^2} \right) \quad L = \left(\frac{D\sigma_{VM}}{\dot{\epsilon}_{eq}^C} \right)^{\frac{1}{3}} \tag{14}$$

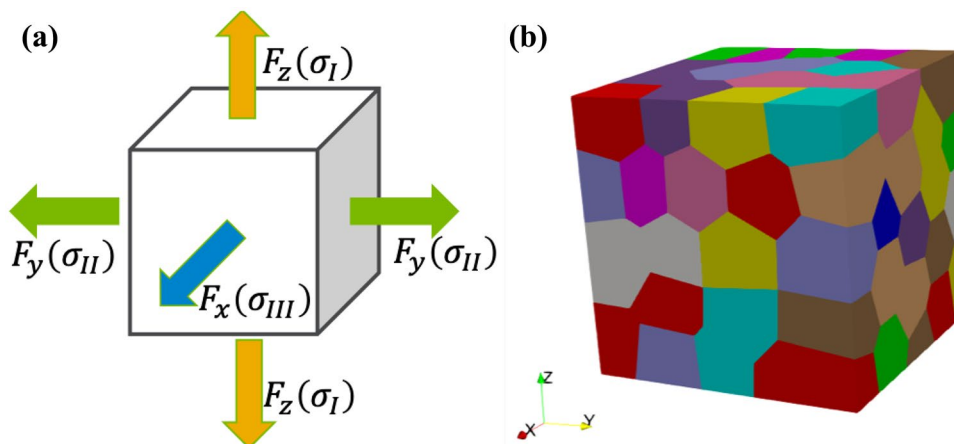
$$f_S = \begin{cases} 1 & \text{if } \frac{a}{b} \leq 0.5 \\ 2 \left(1 - \frac{a}{b} \right) & \text{if } \frac{a}{b} > 0.5 \end{cases}$$

$$q(f) = 2 \log \left(\frac{1}{f} \right) - (1 - f)(3 - f) \tag{15}$$

$$h(\Psi) = \left(\frac{1}{1 - \cos(\Psi)} - \frac{\cos(\Psi)}{2} \right) \frac{1}{\sin(\Psi)} \tag{16}$$

$$m = \text{sign}(\sigma_H) \beta(m) = \frac{(n - 1)[n + g(m)]}{n^2} \tag{17}$$

Fig. 1 **a** Schematic depicting the imposed block-periodic and applied constant force boundary conditions; **b** The representative volume element used in the simulations



$$g(1) = \log(3) - \frac{2}{3} g(-1) = \frac{2\pi}{9\sqrt{3}} g(0) = 0 \quad \alpha_n = \frac{3}{2n} \quad (18)$$

Simulations Setup and Time to Rupture Definition

The simulations imitate the triaxial creep test methodology proposed by Sakane and Hosokawa [9], applying a different constant axial stress on each side of a cubic specimen. Block periodic boundary conditions remove the free surface effects, and constant force boundary conditions mimic the imposed dead-load in creep tests, Fig. 1a. In the simulations, the virtual specimen is a representative volume element including 100 randomly oriented, equiaxed grains, with an average diameter of 60 μm , Fig. 1b. Messner et al. showed that using 100 grains is enough to reproduce the macroscopic material behavior for Grade 91 using block periodic boundary conditions. We used *NEPER* [35] to generate the representative volume element, and the *Coreform* application to generate the mesh. These simulations can impose arbitrary loading conditions, including stress states that are difficult to achieve experimentally.

We ran uniaxial simulations at four stress magnitudes: 60 MPa, 100 MPa, 140 MPa and 180 MPa. The simulations also explore the multiaxial stress space by applying all possible combinations of principal stresses from the list -180 MPa, -140 MPa, -100 MPa, -60 MPa, 0 MPa, 60 MPa, 100 MPa, 140 MPa and 180 MPa, but always including a tensile first principal stress σ_I , i.e., $\sigma_I > 0$, and with a third principal stress satisfying $|\sigma_{III}| \leq \sigma_I$, for a total of ninety-one simulations. To avoid extrapolating beyond the calibration limit of the time to rupture correlation, we only retain virtual experiments generating a creep rupture time within the range of the uniaxial rupture simulations.

We had to select a failure criterion to obtain an objective time to rupture from the simulations. Achieving complete failure in multiaxial, stress-controlled simulations is numerically challenging and computationally expensive.

Creep strain cannot be used as a failure criterion because the triaxiality factor influences creep ductility [36–39]. Dilation, i.e., the fractional volume increase, is associated with the growth of creep cavities, mostly on internal boundary surfaces. Graverend et al. [40] showed that the fractional volume increase is almost stationary during primary and secondary creep and suddenly increases before rupture, suggesting a dilation value can be used as a proxy for creep rupture time. Therefore, we select as failure criterion the time at which the net volume of the simulated RVE increases by 2%, i.e., $t_r^{2\%}$. The calculated net volume increase only includes volume changes induced by the grain-boundary opening. We identified the critical dilation value by performing a sensitivity analysis on the critical cavity volume we associate with failure. The results presented here are insensitive to the critical cavity volume fractions values ranging from 1 to 5%. A dataset containing the simulated stress states and corresponding rupture times is available for download [41]. We assess the accuracy of various effective stress measures against the simulation database assuming $t_r^{2\%}$ accurately represents the rupture time. In this work, uncertainties related to different microstructural features such as grain shape, grain size, texture, etc., or grain boundary cavitation model kinetics and parameters were not considered because of the numerical cost associated with a rigorous uncertainty analysis.

Uniaxial Time to Rupture Correlation

At a fixed temperature a simple creep rupture model can be used to correlate the stress with rupture time:

$$t_r = A(\sigma_{\text{eff}})^n \quad (19)$$

where A and n are material-dependent parameters. Equation 19 is accurate if the rupture time versus stress is linear in log-log space. At 600 $^{\circ}\text{C}$, the Grade 91 creep rupture curve exhibits a change in slope around 100 MPa [42, 43],

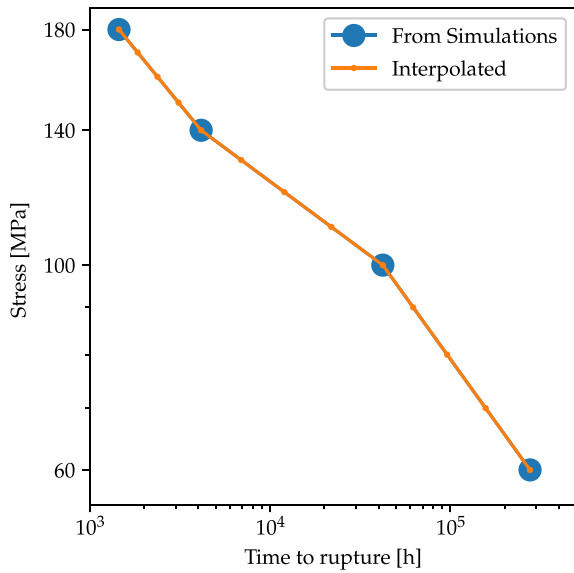


Fig. 2 Piecewise log-linear stress/time to rupture model constructed using the simulated uniaxial creep rupture results for Grade 91 at 600 °C

Table 3 Coefficients of the piecewise log-linear creep rupture and the associated stress ranges constructed using the simulated uniaxial creep rupture results for Grade 91 at 600 °C

stress range	A	n
60 ≤ σ _{eff} < 100	9.73e+11	-3.68
100 ≤ σ _{eff} < 140	2.65e+18	-6.90
140 ≤ σ _{eff} ≤ 180	3.89e+12	-4.18

Stress in MPa, time in h

and the micro-mechanical model replicates this shift. Therefore, the creep rupture model used here captures the uniaxial stress dependence using a piecewise log-linear correlation. All the rupture data (uniaxial and multiaxial) fall within the times covered by this piecewise log-linear rupture correlation, so, the results here only require *interpolating* within the uniaxial rupture model predictions. This approach separates the two problems of extrapolating uniaxial rupture data in time (not addressed here) and using uniaxial and biaxial rupture data to predict failure under triaxial stresses (the focus of this work). Table 3 shows the calibrated coefficients for all stress ranges. Figure 2 depicts the piecewise log-linear time to rupture relationship.

Experimental Data

To assess the effective stress models against experimental data, we consider three structural, high-temperature materials: stainless steel 304 (*SS304*), stainless steel 316

(*SS316*) and Inconel 600 (*IN600*). These materials have a face-centered cubic structure, and we used biaxial creep experimental data and uniaxial time to rupture correlations from [17–19], for *SS304*, *SS316* and *IN600*, respectively. Experimental data and the uniaxial correlation coefficients are available for download at [41].

Effective Stress Measures Definitions and Calibration

This work considers all the effective stress measures mentioned in the introduction, defined by Eqs. 20–26, and three additional effective stresses:

1. The maximum between the tensile first principal stress and the von Mises stress, σ_{max(σ_{VM},σ_I)} (Eq. 27)
2. An extension of the Huddleston stress using σ_{Sd} as prefactor instead of σ_{VM}, σ_{NEW¹} (Eq. 28)
3. A further modification to Huddleston stress, where both the prefactor and the exponential term are function of σ_{Sd}, σ_{NEW²} (Eq. 29)

In these equations α and β are material-dependent parameters, and SS is the distance from the origin in stress space, i.e., SS = √(σ_I² + σ_{II}² + σ_{III}²). All the effective stress measure are defined to be non-negative. The bounds and constraints for the effective stress parameters in Eqs. 20–29 are:

- 0 ≤ α ≤ 1 for Eq. 22,
- 0 ≤ β ≤ 1 for Eqs. 25 and 26,
- 0 ≤ α ≤ 1, 0 ≤ β ≤ 1, with α + β = 1, for Eq. 23, and
- 0 ≤ α ≤ 1 and β ≥ 0 for Eqs. 24, 28, 29.

The material parameter α is always the coefficient related to the tensile first principal stress, while the parameter β is always related to the first stress invariant. The material parameters α and β should be defined so that the stress measure is always positive. Since simulations include the evolution of creep damage via the grain boundary cavitation model, the calculated time to rupture, and thus the optimized material parameters, implicitly account for material damage evolution. Furthermore, since the calculated rupture time is based on a critical void volume fraction, results are independent from the macroscopically observed creep ductility variation.

$$\sigma_{Tresca} = \sigma_I - \sigma_{III} \tag{20}$$

$$\sigma_{VM} = \sqrt{\frac{(\sigma_I - \sigma_{II})^2 + (\sigma_I - \sigma_{III})^2 + (\sigma_{II} - \sigma_{III})^2}{2}} \tag{21}$$

$$\sigma_{Sd}(\alpha) = \alpha \langle \sigma_I \rangle + (1 - \alpha) \sigma_{VM} \tag{22}$$

$$\sigma_{HLM}(\alpha, \beta) = \alpha \langle \sigma_I \rangle + \beta |I_1| + (1 - \alpha - \beta) \sigma_{VM} \tag{23}$$

$$\sigma_{Hudd}(\beta) = \sigma_{VM} \exp \left[\beta \left(\frac{I_1}{SS} - 1 \right) \right] \tag{24}$$

$$\sigma_{RCC_{VM}}(\beta) = (1 - \beta) \sigma_{VM} + \beta I_1 \tag{25}$$

$$\sigma_{RCC_{Tresca}}(\beta) = (1 - \beta) \sigma_{Tresca} + \beta I_1 \tag{26}$$

$$\sigma_{\max(\sigma_{VM}, \langle \sigma_I \rangle)} = \max(\sigma_{VM}, \langle \sigma_I \rangle) \tag{27}$$

$$\sigma_{NEW^1}(\alpha, \beta) = \sigma_{Sd}(\alpha) \exp \left[\beta \left(\frac{I_1}{SS} - 1 \right) \right] \tag{28}$$

$$\sigma_{NEW^2}(\alpha, \beta) = \sigma_{Sd}(\alpha) \exp \left[\beta \left(\frac{I_1}{\sigma_{Sd}(\alpha)} - 1 \right) \right] \tag{29}$$

In the following, we distinguish between effective stress measures with an explicit dependence on the first stress invariant I_1 and those that do not, i.e., measures with and without a β parameter. This distinction is subtly different than stating an effective stress measure does or does not depend on pressure. Of the invariants used to define the effective stress measures considered here, σ_{Tresca} and σ_{VM} do not depend on the pressure at all—they are strictly functions of the deviatoric stress and superimposing an arbitrary pressure does not change the values of these invariants. The other invariants— $\langle \sigma_I \rangle$, I_1 , and σ_{SS} —do vary with the pressure. However, only I_1 scales linearly with an increase in pressure. If the material has a failure mechanism that scales with the applied pressure, then I_1 best describes this volumetric mechanism. However, other invariants, including σ_I , partly account for the pressure dependence, particularly for moderately triaxial stress states.

We minimize the mean absolute relative error to find the best-fit parameters (for the models with parameters). The creep rupture life spans several orders of magnitude and the relative error normalizes these differences. For example, a 100 h error is much more severe when considering a creep rupture time of 1000 h versus 100000 h. The relative error definition is:

$$e_{rel} = \frac{t_p - t_r}{t_r} \tag{30}$$

where t_r is the real time to rupture and t_p is the rupture time predicted using Eq. 19 and the calibrated coefficients. In the following discussion, we also define the mean absolute relative error as:

$$e = \frac{1}{N} \sum_{i=1}^N ||w_i \cdot e_{rel,i}|| \tag{31}$$

where i is the index referring to a specific datapoint, w_i is a weight factor, and N is the total number of training data. For simulations, the weight $w_i = 1$. For repeated experiments, $w_i = \frac{1}{M}$, where M is the number of experiments with the same stress state.

The effective stress parameters were calibrated twice, once using only biaxial simulation results (i.e., stress states with two nonzero principal stresses) and then once again using all multiaxial simulation results, including triaxial loads. Henceforth, we will refer to the first case as *Fit2D* and to the second case as *Fit3D*. For experiments, the effective stress parameters were calibrated once for each material using all the available experimental results, which only includes biaxial stress states.

Two of the investigated effective stress measures, i.e., $\sigma_{RCC_{VM}}$ and $\sigma_{RCC_{Tresca}}$, can return negative values if $\beta > 0$ and I_1 is sufficiently negative. To deal with this, if during the optimization a negative effective stress value is returned, then a very large penalty, i.e., 1×10^6 , is added to the error, e . This approach provides effective stress parameters always returning a positive effective stress for all the training data. Constraints are imposed using the Lagrange multiplier approach, and hence the Lagrangian function to optimize is:

$$f(x, \lambda) = e + \sum_q \lambda_q g_q(x) \tag{32}$$

where x is the vector of material parameters, λ is the vector of Lagrange multipliers, and g are the constraints.

We optimized the parameter using the constrained trust-region algorithm available in the SciPy [44] package. The trust region method is a local optimization technique that at each step searches for a minimum of the cost function within a region of size Δ . Using a quadratic approximation function the trust algorithm repeatedly solves the following problem until the norm of the step, s , is below a certain tolerance:

$$\begin{aligned} \text{minimize } m(s) &= f(x) + s^T \cdot \nabla f_x + \frac{1}{2} s^T B_x s \\ \text{subject to: } & ||s|| \leq \Delta \end{aligned} \tag{33}$$

where x is the solution vector at the previous iteration and includes Lagrange multipliers, B is the Hessian matrix, and s is the step vector. The trust region algorithm increases or reduces Δ based on the ratio $\frac{\Delta f}{\Delta m}$ calculated using two consecutive steps. For a more detailed description of the trust region method, refer to [45].

The trust region method is a local optimizer; thus to ensure convergence to a global minimum, we used multiple initial guesses evenly distributed in the feasible region of the solution

Table 4 The optimum value of the calibrated material parameters

Measure	Fit2D		Fit3D	
	α	β	α	β
σ_{VM}				
σ_{Tresca}				
σ_{Sd}	0.232		0.307	
σ_{HLM}	0.181	0.017	0.249	0.020
σ_{Hudd}		0.002		0.022
$\sigma_{RCC_{VM}}$		0.052		0.097
$\sigma_{RCC_{Tresca}}$		0.011		0.098
$\sigma_{\max((\sigma_I), \sigma_{VM})}$				
σ_{NEW^1}	0.213	0.001	0.302	0.000
σ_{NEW^2}	0.185	0.017	0.232	0.026

Column *Fit2D* contains the parameters calibrated using biaxial stress states. The parameters in column *Fit3D* are optimized using biaxial and triaxial stress states. Coefficients α and β are always related to the maximum tensile principal stress and to the first stress invariant, respectively

space and then took the lowest, best minimum resulting from these grid calculations.

Results and Discussion

Extrapolating from Biaxial Data Using Simulated Creep Rupture Data

In this section, we use the simulated creep rupture life for Grade 91 at 600 °C to assess the accuracy of biaxial calibrated effective stress measures when predicting the rupture time for triaxial stress states. Table 4 shows the optimized material parameters calibrated against simulation results for two case: (i) when *only* biaxial creep rupture data are included in optimization dataset, i.e., *Fit2D*, and (ii) when the optimization includes both the biaxial *and* triaxial stress states, i.e., *Fit3D*.

We then compute the relative mean error for three cases: (i) using the effective stress parameters optimized using *only* biaxial data and the associated error against the biaxial simulations, i.e., *Fit2D-data2D*, (ii) using the biaxial calibrated parameters and the mean relative error computed using both biaxial *and* triaxial data, i.e., *Fit2D-data3D*, and (iii) using the optimal effective stress parameters optimized using biaxial *and* triaxial data and the error against both the biaxial and triaxial simulations, i.e., *Fit3D-data3D*. Table 5 summarizes the synthetic creep rupture times used for calibrating material parameters and for computing the mean absolute relative error for the three different cases.

The first case, *Fit2D-data2D*, mimics the current engineering approach, the second case, i.e., *Fit2D-data3D*, provides insights on the extrapolation accuracy of the

Table 5 Synthetic creep rupture used for the calibration process and to compute the mean absolute relative error

	Calibration		Mean absolute relative error	
	Biaxial	Triaxial	Biaxial	Triaxial
<i>Fit2D-data2D</i>	X		X	
<i>Fit2D-data3D</i>	X		X	X
<i>Fit3D-data3D</i>	X	X	X	X

Table 6 Mean relative errors for all the measures

Measure	Fit2D		Fit3D
	data2D	data3D	data3D
σ_{VM}	0.24	3.98	3.98
σ_{Tresca}	0.35	3.94	3.94
σ_{Sd}	0.10	0.37	0.22
σ_{HLM}	0.09	0.36	0.21
σ_{Hudd}	0.19	3.22	0.68
$\sigma_{RCC_{VM}}$	0.14	0.73	0.27
$\sigma_{RCC_{Tresca}}$	0.35	2.65	0.39
$\sigma_{\max((\sigma_I), \sigma_{VM})}$	0.24	0.59	0.59
σ_{NEW^1}	0.08	0.39	0.22
σ_{NEW^2}	0.09	0.35	0.21

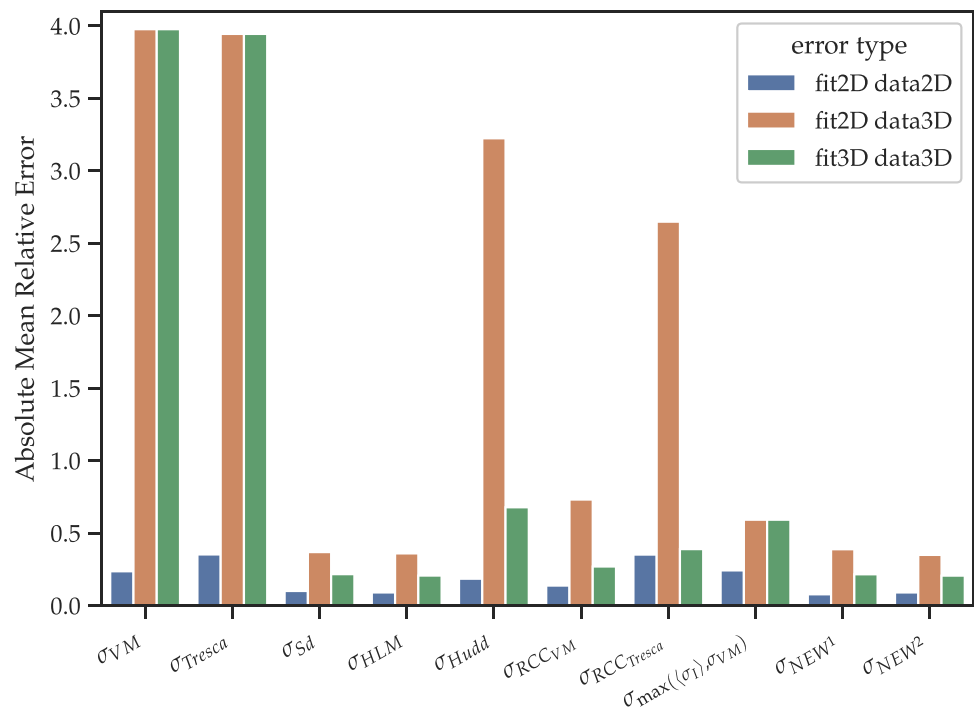
The column headers *fit2D* and *fit3D* identify the data used for effective stress coefficient optimization

investigated effective stress measures, and the third case, i.e., *Fit3D-data3D*, evaluates the benefits of performing creep experiments for triaxial stress states. Table 6 summarizes the resulting mean absolute relative errors.

Figure 3 visually compares the three different errors for all the measures.

We start by analyzing the results for the *Fit2D-data2D* case. Blue bars in Fig. 3 represent the mean absolute relative error for this case. The results show that all the effective stress measures perform equally well, with σ_{Tresca} generating the largest error of 35%. For creep rupture, errors up 100% can be acceptable, given that heat-to-heat variability in rupture life commonly exceeds a factor of 2, and it can reach a factor of 10 for low-stress, high temperature conditions [46]. Among the measures available in the literature, σ_{Sd} and σ_{HLM} generate the smallest errors, i.e., 10%, 9%, respectively, and the measure proposed by Huddleston is in the middle at 19%. The measures used by *RCC-MRx* also exhibit small errors. The fact that all the measures are about equally effective for the *Fit2D-data2D* case may explain why the scientific and engineering communities do not agree on the best effective stress measure, and why different high-temperature design codes and fitness-for-service manuals adopt different effective stress measures.

Fig. 3 Errors bar plot for the investigated effective stress measures obtained using simulation's results for Grade 91 at 600 °C, and the time to 2% void volume fraction as a proxy for failure. In the legend *fit2D* and *fit3D* identify the data used for fitting. Also *data2D* and *data3D* refers to which data have been used to calculate the error. The suffix *2D* refers *only* to biaxial data, the suffix *3D* refers to biaxial *plus* triaxial data



When considering the *Fit2D-data3D* case, i.e., when using biaxial calibrated effective stress coefficients to predict the creep life for triaxial stress states, not all measures behave well. Orange bars in in Fig. 3 represent this case. In this situation, σ_{VM} , σ_{Tresca} , σ_{Hudd} and $\sigma_{RCC_{Tresca}}$ generate errors larger than 250%. In contrast, σ_{Sd} and σ_{HLM} produce very small errors, i.e., 37% and 36%, respectively.

None of the measures available in the literature have both good extrapolation ability and an explicit, consistent dependence on the first invariant. Among the measures with good extrapolation ability, the one proposed by Sdobyrev does not include the first stress invariant, the measure introduced by Hayhurst does not distinguish between positive and negative values of the first stress invariant, and $\sigma_{RCC_{VM}}$ could return a negative effective stress for some values of applied stress, which is undesirable as it means it cannot be used to predict rupture life for an arbitrary state of stress. The Huddleston effective stress is the only one that discerns between positive and negative values of the first stress invariant, but it does not accurately extrapolate from biaxial to triaxial stress states. Therefore, we introduce two additional effective stress measures, both using Huddleston exponential form and the Sdobyrev measure: σ_{NEW1} and σ_{NEW2} . The only difference between the two proposed measures is the effective stress value used to scale the first stress invariant inside the exponent. The first measure uses the term proposed by Huddleston, i.e., SS , the second one uses the Sdobyrev stress. Both formulations are inspired by the definition of stress triaxiality, i.e., I_1/σ_{VM} , but use as a scaling factor an effective

stress returning a nonzero value for pure hydrostatic loading cases. When considering the *Fit2D-data3D* case, both the proposed effective stress measures produce very small errors and possess good extrapolation ability, with σ_{NEW2} generating slightly lower mean absolute relative error than σ_{NEW1} .

Lastly, we present results for the hypothetical case where real triaxial creep experimental data are available, i.e., *Fit3D-data3D*. Green bars in in Fig. 3 represent this scenario. Results obtained using simulated creep rupture times show the availability of experimental triaxial creep rupture data would significantly increase the accuracy of predictions for all the effective stress measures with material-specific parameters. In most cases, the error would drop below 50%, thus greatly improving creep rupture life estimates. This would lead to significantly more accurate creep rupture predictions under multiaxial stress states in structural components

Most effective stress measures have material-specific parameters requiring calibration against at least some multiaxial rupture data. From the literature models, only σ_{Tresca} and σ_{VM} do not have configurable parameters and these are both very inaccurate when compared to simulated triaxial rupture data. An accurate, parameter-free effective stress measure could be useful, for example in preliminary design assessments to evaluate the suitability of new materials. Inspired by the good extrapolation ability of the Sdobyrev measure, we proposed an additional parameter-free effective stress, $\sigma_{max}((\sigma_1), \sigma_{VM})$. Results shows $\sigma_{max}((\sigma_1), \sigma_{VM})$ would produce small errors for both the *data2D*, *data3D* cases, 24% and 59%, respectively.

Fig. 4 Scatter plot of the signed relative error for all simulation results. Effective stress parameters were calibrated using only biaxial stress states

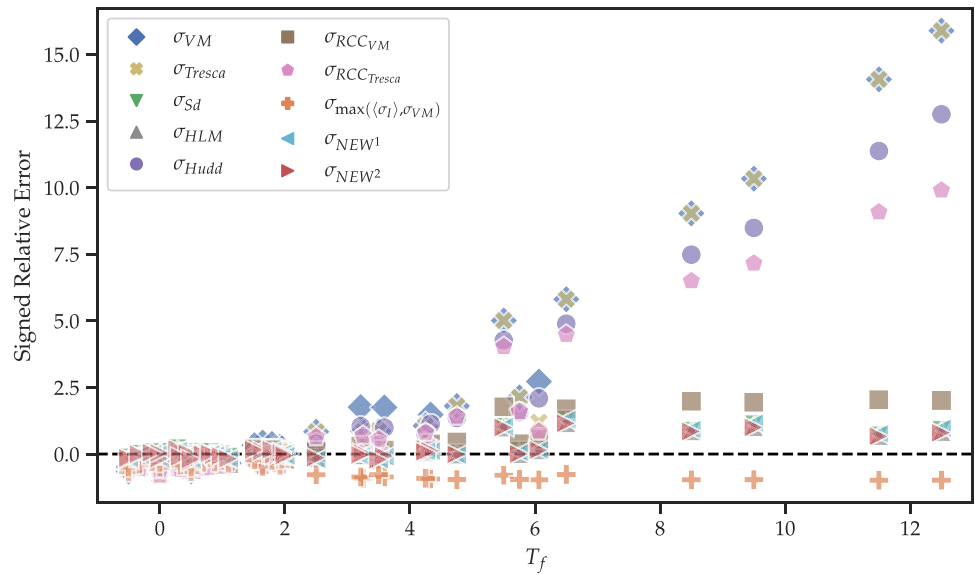


Fig. 5 Enlarged view of Fig. 4 emphasizing medium and low triaxiality regimes

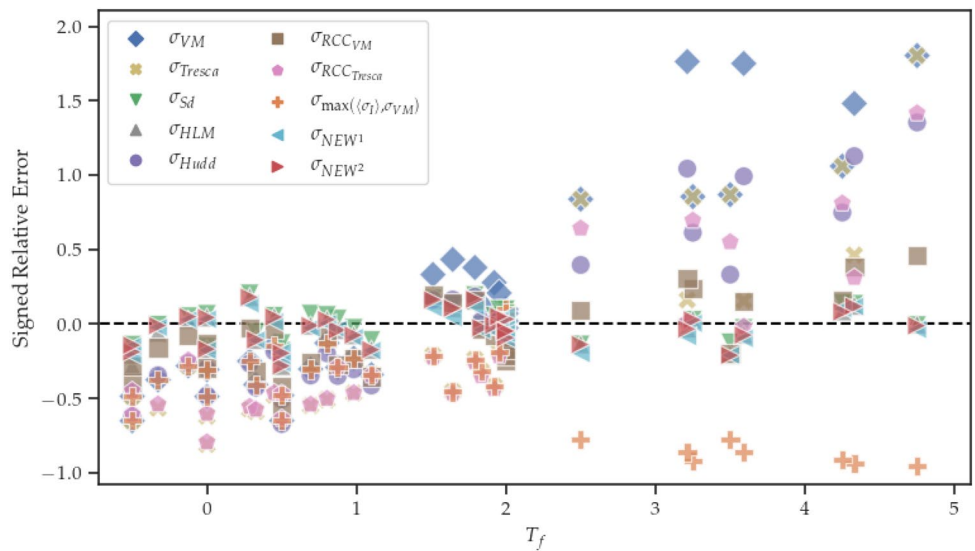


Figure 4 depicts the signed relative error as function of the triaxiality factor for the *Fit2D-data3D* case. According to Eq. 30, a positive error means the model overestimates the creep rupture life, and -1 is the lower bound.

These results show the error depends on the triaxiality factor and on the choice of the effective stress measure. The triaxiality space can be divided into three regions, low (i.e., $T_f \leq 2$), moderate (i.e., $2 < T_f \leq 5$), and high (i.e., $T_f > 5$). In the low-triaxiality regime, the error generated by triaxial and biaxial stress states is comparable. Using biaxial calibrated measures to estimate the creep life for triaxial stress states within this regime does not introduce large errors. Results in the high-triaxiality regime suggest measures can be divided into two categories: (i) measures whose error increases with the triaxiality factor, i.e., σ_{VM} , σ_{Tresca} , σ_{Hudd} ,

and $\sigma_{RCC_{Tresca}}$, and (ii) measures whose error saturates at high triaxiality values, i.e., σ_{Sd} , σ_{HLM} , σ_{NEW1} , σ_{NEW2} , $\sigma_{RCC_{VM}}$, and $\sigma_{\max(\langle\sigma_I\rangle, \sigma_{VM})}$. Notice that data points for σ_{NEW1} , σ_{NEW2} , σ_{Sd} , σ_{HLM} are difficult to distinguish in Fig. 4 because they overlap. The current analysis does not rigorously demonstrate that this saturation trend provides an upper bound on error for highly triaxiality load conditions, but it is suggestive.

The low- and moderate-triaxiality regimes are the most relevant to engineering applications. Figure 5 provides an enlarged view of the signed relative error within these regimes. Triaxiality factors above five are typical of very sharp notch geometries and cracks [47] and therefore are likely precluded in the initial design of a component. Furthermore, some high-temperature design codes, such as Section III, Division 5 of the ASME BPV, limit the allowable

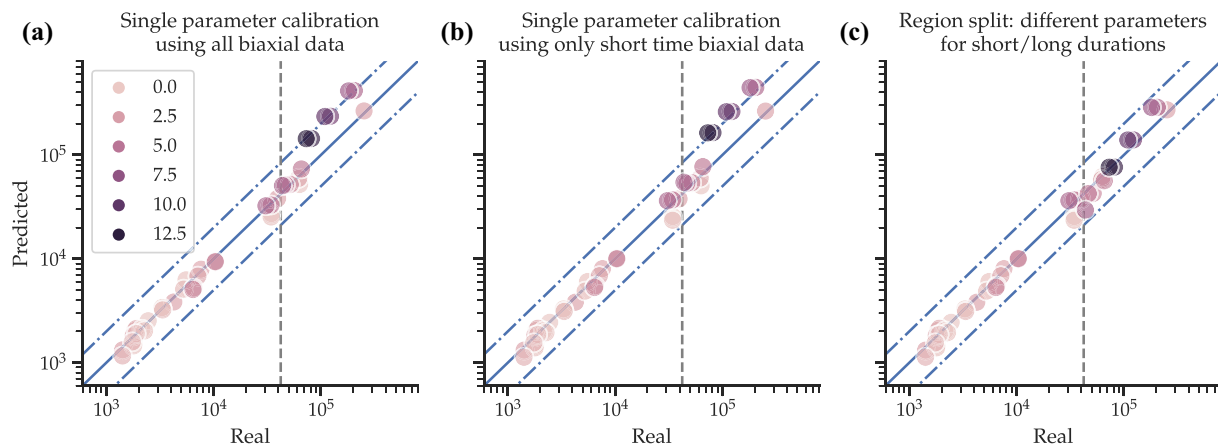


Fig. 6 The predicted versus the simulated creep rupture time generated using the σ_{NEW1} effective stress measures calibrated using: **a** all available biaxial data, **b** only short-time biaxial data, i.e., $t_r^{2\%} \leq 42160$ h, and **c** different parameters for short and long creep

stress triaxiality. In the moderate-triaxiality regime, the measures exhibiting a saturating error are far more accurate than the others. Figure 5 shows σ_{Sd} , σ_{HLM} , σ_{NEW1} , and σ_{NEW2} produce signed relative errors within $\pm 25\%$ band. Furthermore, $\sigma_{\max(\langle \sigma_I \rangle, \sigma_{VM})}$ always provides conservative results, e.g., negative signed relative errors, particularly with larger margin in the intermediate triaxiality regime. These results suggest that when selecting an effective stress measure for components designed to operate at moderate triaxiality values, one should prioritize a measure exhibiting a saturating behavior. The results presented in this section do not account for the experimentally observed creep rupture life variability because our model is deterministic.

Extrapolation in Time

Creep rupture experiments, including biaxial tests, are commonly available only for short rupture times where dislocation creep is the dominant mechanism. Designers must therefore calibrate uniaxial rupture correlations and parameters for effective stress measures against comparatively short-term data and then extrapolate in time to reach realistic component design lives. Empirically, the uniaxial creep rupture correlation of many materials exhibits a change in slope below a particular stress value, see for instance [42, 43]. This shift in slope corresponds to a physical mechanism change: at low stress levels, diffusion creep becomes the dominant deformation and damage mechanism. As mentioned previously, predicting the shift in the *uniaxial* creep rupture correlation is not the focus of this paper. We did assess the accuracy of the effective stress measures against the numerical data applying an inaccurate uniaxial rupture correlation that simply extrapolates from the short-term data

rupture times. Dash dotted lines identify the $\pm 100\%$ limits, the vertical dashed line separates the short- and long-time regions. The colors represent the triaxiality factor of each virtual experiment

log-linearly, missing the mechanism shift. When using this uniaxial rupture correlation the effective stress measures do not accurately predict the long-term multiaxial failure simulations. This result is tautological—an inaccurate uniaxial rupture correlation produces similar errors even for uniaxial failure. However, the question of extrapolation from short-term biaxial data to long-term triaxial failure is relevant to this work.

In this section, we use the simulated creep-rupture data for Grade 91 to investigate: (i) the loss in accuracy when predicting the long-time multiaxial creep rupture time using effective stress measures calibrated *only* against short-time biaxial data, and (ii) the potential benefits of performing long-time biaxial creep rupture experiments. For the remainder of this section, we refer to short-time creep rupture data as all virtual experiments with a simulated creep rupture time $t_r^{2\%} \leq 42160$ h, which is the creep rupture time for the uniaxial case at 100 MPa. At 600 °C, this value indicates the mechanism shift from dislocation to diffusional creep based both on the underlying crystal plasticity model [24, 48] and on experimental data [42, 43]. In what follows, we present results only for the σ_{NEW1} effective stress measure. However, we obtained similar results for all other effective stress measures with configurable parameters.

Figure 6a–c shows the predicted versus the simulated creep rupture time for three cases: (i) when calibrating the effective stress measure parameters using *all* available biaxial simulation data, (ii) when calibrating effective stress measure parameters using *only* short-time biaxial data, and (iii) when calibrating effective stress measure parameters separately for long and short-time creep rupture times, using different parameters sets in the two regions. This final case corresponds to a region-split approach for uniaxial rupture correlations. Table 7

Table 7 The calibrated effective stress measure parameters for three cases: (i) using all the available simulated biaxial creep rupture times (*Fit2D*), (ii) using only biaxial creep rupture simulations with a $t_r^{2\%} \leq 42160$ h (short-time), and (iii) using only biaxial creep rupture simulations with a $t_r^{2\%} > 42160$ h (long-time)

Measure	Combined		Short-time		Long-time	
	α	β	α	β	α	β
σ_{NEW^1}	0.213	0.001	0.195	0.001	0.354	0.000

Table 8 The effective stress parameters calibrated using biaxial experimental data for different materials

Measure	SS 304		SS 316		Inconel 600	
	α	β	α	β	α	β
σ_{VM}						
σ_{Tresca}						
σ_{Sd}	0.727		0.478		0.494	
σ_{HLM}	0.000	0.285	0.352	0.051	0.000	0.201
σ_{Hudd}		0.014		0.225		0.022
$\sigma_{RCC_{VM}}$		0.281		0.188		0.199
$\sigma_{RCC_{Tresca}}$		0.321		0.309		0.178
$\sigma_{\max((\sigma_r), \sigma_{VM})}$						
σ_{NEW^1}	0.547	0.010	0.472	0.002	0.369	0.018
σ_{NEW^2}	0.000	0.305	0.375	0.050	0.013	0.205

Coefficients α and β are always related to the maximum tensile principal stress and to the first stress invariant, respectively

summarizes the calibrated parameters for σ_{NEW^1} for the three cases. The first case is exactly the same as the *Fit2D-data3D* case presented in Sect. “Extrapolating from Biaxial Data Using Simulated Creep Rupture Data,” the second case represents the current engineering approach where effective stress measures are used beyond their calibration range, and the third case provides insight into how effective stress models depend on the active creep mechanism. In Fig. 6, the vertical dashed lines separate the short and long-time regions, the diagonal dashed-dotted lines identify the $\pm 100\%$ limits, and colors represent the triaxiality factor, T_f , associated with each virtual experiment.

Results in Fig. 6a, b are almost identical with errors concentrated in the high triaxiality regimes, i.e., $T_f > 5$ and for long rupture times. There is almost no difference in the effective stress parameters calibrated against the entire biaxial dataset and the parameters calibrated only against the short-term data (see Table 7). Note that only three biaxial virtual experiments are available within the long-time creep rupture region in the virtual dataset. However, the abundance of triaxial data in the long-time region demonstrates that an accurate effective stress metric calibrated using only short-time, biaxial creep rupture data can be used beyond its calibration range without generating errors beyond the $\pm 100\%$ limits.

Figure 6c demonstrates lower errors in the long-time creep rupture regime when compared to results in Fig. 6a, b. This suggests the effective stress parameters depend on the dominant creep damage mechanism, and more accurate effective stress models could be developed if long-term biaxial rupture data were available.

Comparison to Biaxial Experimental Test Data

This section considers whether the results of the analysis in the previous sections hold for other materials and against experimental biaxial rupture test data. Table 8 lists the best-fit effective stress parameters calibrated against the *experimental* database described above. Figure 7 is a bar plot comparing the mean absolute relative error of each measure against the database, and Table 9 summarizes the results in the bar plot. Furthermore, each scatter plot in Fig. 8 depicts the signed relative error for a single effective stress measure calculated against all materials.

The results show that not all effective stress measures accurately predict the creep rupture life for all the materials. All the measures produce comparable, low errors for *SS316* and *IN600*, but some measures behave better than others. For both materials σ_{NEW^1} is the most accurate and σ_{VM} is the least accurate. For *SS316*, σ_{NEW^2} and σ_{HLM} exhibit a mean absolute relative error 1% larger than σ_{NEW^1} . For *IN600*, $\sigma_{RCC_{Tresca}}$ and

Fig. 7 Bar plots of the mean relative error against the experimental test data for effective stress measures calibrated against the experimental data

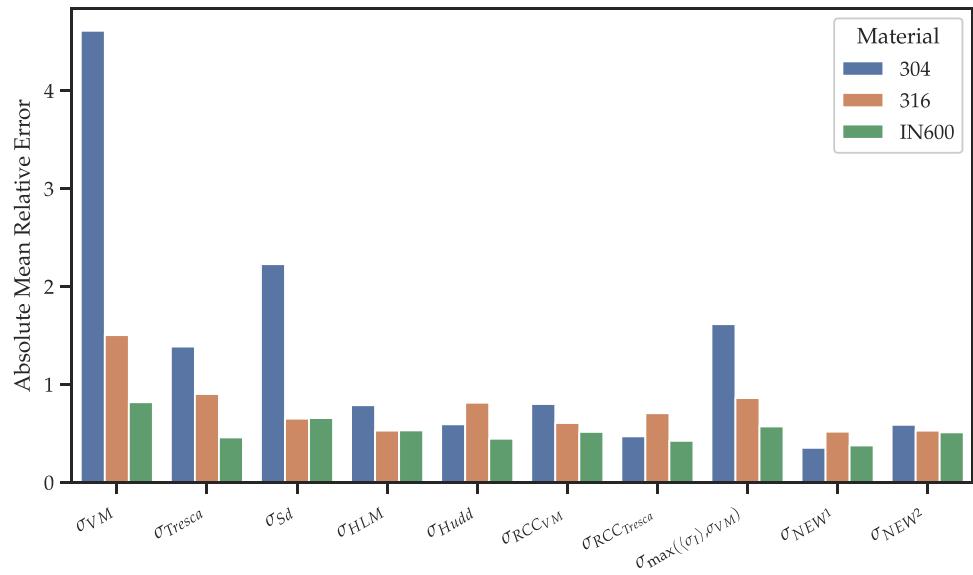


Table 9 The mean relative absolute error generated using experimentally calibrated effective stress measures

	SS 304	SS 316	Inconel 600
σ_{VM}	4.612	1.504	0.819
σ_{Tresca}	1.387	0.902	0.459
σ_{Sd}	2.228	0.651	0.657
σ_{HLM}	0.788	0.529	0.531
σ_{Hudd}	0.593	0.814	0.446
$\sigma_{RCC_{VM}}$	0.800	0.606	0.516
$\sigma_{RCC_{Tresca}}$	0.470	0.707	0.424
$\sigma_{\max((\sigma_I), \sigma_{VM})}$	1.616	0.861	0.571
σ_{NEW1}	0.353	0.518	0.377
σ_{NEW2}	0.588	0.528	0.511

σ_{Hudd} are the second and third most accurate measures. Scatter plots in Fig. 8 reveal a higher accuracy does not guarantee a lower chance of overpredicting the creep rupture time. For *SS316*, $\sigma_{RCC_{Tresca}}$ is less accurate than σ_{NEW2} and σ_{HLM} , but the former has a lower maximum signed relative error, making it more conservative. The same consideration holds for *IN600* and *SS304* when comparing σ_{NEW1} with $\sigma_{RCC_{Tresca}}$.

All the measures not explicitly including the hydrostatic stress overestimate the creep rupture life for *SS304*, particularly for higher triaxiality values, with the worst measures being σ_{VM} , σ_{Sd} and $\sigma_{\max((\sigma_I), \sigma_{VM})}$. As we note above, measures including σ_I do include some dependence of the pressure. However, empirically, measures that explicitly include I_1 in their formulation perform better than measures that do not explicitly include it.

The fitted coefficients of σ_{NEW2} for *SS304* reveal this measure has undesirable behaviors under some conditions. If $\alpha = 0$, then $\sigma_{Sd} = \sigma_{VM}$, and hence purely negative

hydrostatic stress state would result in an infinite rupture time, while any pure positive hydrostatic stress state would result in a zero rupture time. The above suggests restrictions are needed on the α parameter and/or the stress state to prevent the occurrence of doubly pathological conditions when using σ_{NEW2} . Furthermore, the values in Table 8 also demonstrate that effective stress parameters are highly material-dependent. Using material independent parameters might lead to drastically inaccurate results, or to unnecessary conservative safety factors.

For biaxial experimental data, σ_{Sd} and σ_{HLM} are less accurate than σ_{NEW1} , suggesting the σ_{NEW1} might be more resilient against typical experimental and heat-to-heat variations. Furthermore, the smaller signed relative error generated by σ_{NEW1} , σ_{NEW2} and σ_{Hudd} compared to σ_{HLM} suggests a nonlinear dependence of the creep rupture time on the hydrostatic stress. However, the results for $\sigma_{RCC_{Tresca}}$ negate this idea, at least for the low triaxiality regime. Lastly, the parameter-free effective stress measure, $\sigma_{\max((\sigma_I), \sigma_{VM})}$, does not always produce conservative creep rupture estimates, particularly for *SS304*. Therefore, the proposed parameter-free measure is only adequate to evaluate the creep rupture life for materials with a low sensitivity to the hydrostatic stress, in this case *SS316* and *IN600*.

The experimental database used in this comparison is the same data used by Huddleston (excluding uniaxial stress states, where present) to develop and calibrate his model. However, he tuned the model to produce conservative estimates of rupture time first, and only secondly to try to best-fit the biaxial rupture data. This approach is reasonable for an engineering design method and partly explains why his measure is comparatively inaccurate using our criterion, which aims only to accurately represent the biaxial rupture data. More accurate effective stress measures

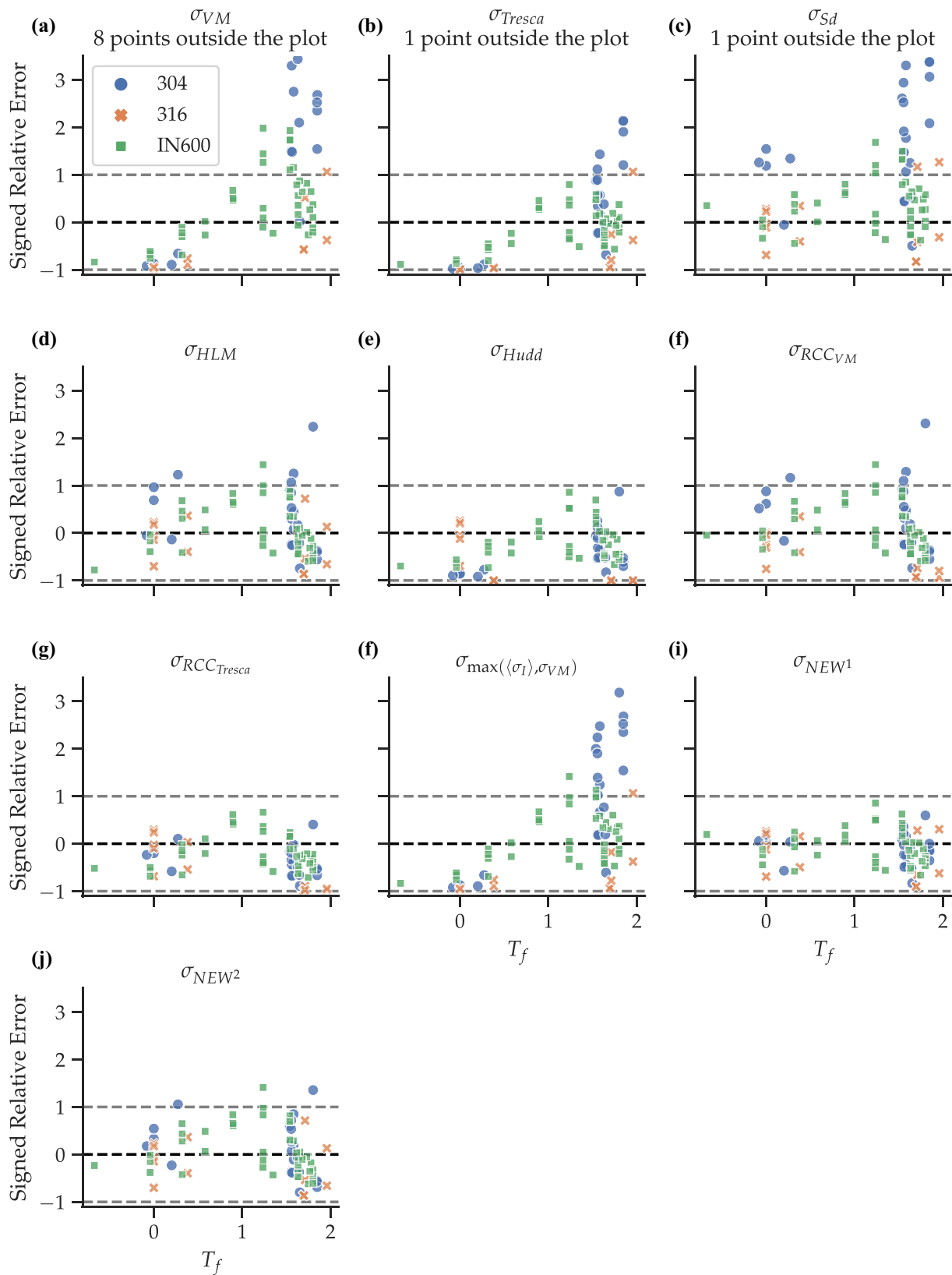


Fig. 8 Scatter plots of the signed relative error for each stress measure. Some of the effective stress measures produce errors outside the plot range for *SS304*. For such cases, the number of missing point is noted in the title. All sub-plots share the same horizontal and vertical axis

could lead to better quantification of design uncertainty and margin, potentially leading to more efficient component designs.

Conclusions

In this work, we used a physically motivated finite element, crystal plasticity model for Grade 91 steel to perform virtual creep experiments for triaxial stress state conditions that cannot be easily achieved experimentally. The simulation results were used to evaluate the error in using common effective stress models to extrapolate from biaxial to triaxial loading conditions and to evaluate the potential benefits of obtaining true triaxial creep rupture test data. Based on these data and analysis, we also proposed three additional effective stress measures, one of which does not require calibrating parameters against multiaxial rupture data. Trends observed in the simulation results were confirmed against experimental biaxial creep rupture test on two austenitic steels *SS304*, *SS316*, and one Nickel-based alloy, *IN600*. The results are generally applicable to other materials with a cubic crystal structure. However, the methodology presented in this manuscript is applicable to any material system. Provided an accurate micromechanical model is available, the techniques developed here could be used to identify the best extrapolating effective stress measures for other crystal systems. Our specific conclusions are:

- For low triaxial stress states, i.e., $T_f \leq 2$, all the effective stress measures that explicitly include the first stress invariant (i.e., those with a parameter β as defined in this work) produce comparable results.
- Some effective stress measures are significantly more accurate than others in the high triaxiality region, i.e., $T_f > 5$. These measures are also generally more accurate in the intermediate regime, i.e., $2 < T_f \leq 5$, though differences between the measures are smaller.
- Based on the numerical and experimental data collected here, the stress measure $\sigma_{NEW1} = \sigma_{Sd}(\alpha) \exp\left[\beta\left(\frac{I_1}{SS} - 1\right)\right]$ is the most suitable measure for assessing multiaxial creep rupture among all the stress measures considered in this work. The model is the most accurate when 3D data are available (i.e., from the crystal plasticity simulations) and is the best at extrapolating from 2D data to 3D rupture predictions.
- Effective stress parameters are substantially material dependent; using universal parameters for different materials might lead to large errors and possibly non-conservative predictions.
- The proposed parameter-free stress measure, i.e., $\sigma_{\max((\sigma_T), \sigma_{VM})}$, produces acceptable creep rupture life

predictions for materials where the rupture life is less sensitive to the hydrostatic stress—316 SS and Inconel 600 for the materials considered here.

- Triaxial creep test data, while difficult to collect experimentally, could generally improve the accuracy of effective stress models, including σ_{NEW1} .
- Effective stress measures can extrapolate in time—measures calibrated against short term rupture data remain accurate when compared to failure data for long-term multiaxial rupture simulations, provided that the mechanisms for short-term and long-term rupture are similar. However, long-term biaxial or multiaxial rupture data would further improve the accuracy of effective stress models.

Creep data for higher triaxiality ratios could improve the accuracy of effective stress measures. Establishing a correlation between creep crack growth data and failure under constant load for highly triaxial stress states could provide this type of data, as could additional micromechanical modeling for other materials. Furthermore, machine learning technique, such as Gaussian process regression, could be used to estimate the uncertainty of the predictions derived here [49].

Acknowledgements The research was sponsored by the US Department of Energy, under Contract No. DEAC02-06CH11357 with Argonne National Laboratory, managed and operated by UChicago Argonne LLC and Contract No. DE-AC07-05ID14517 with Idaho National Laboratory, managed and operated by Battelle Energy Alliance. Programmatic direction was provided by the Office of Nuclear Reactor Deployment of the Office of Nuclear Energy. The authors gratefully acknowledge the support provided by Sue Lesica, Federal Manager, Advanced Materials, Advanced Reactor Technologies (ART) Program, Diana Li, Federal Manager, Microreactor Program, and John H. Jackson of Idaho National Laboratory, National Technical Director, Microreactor Program.

Declarations

Conflict of interest The authors declare no competing interests.

References

1. Katz A, Ranjan D (2019) Advances towards elastic-perfectly plastic simulation of the core of printed circuit heat exchangers. In: Proceedings of the 2019 ASME pressure vessels and piping conference, vol 58943, American Society of Mechanical Engineers, pp PVP2019-93807
2. Rovinelli A, Messner MC, Guosheng Y, Sham TL (2019) Initial study of notch sensitivity of Grade 91 using mechanisms motivated crystal plasticity finite element method. Tech. Rep., Argonne National Laboratory ANL-ART-171
3. Hayhurst D (1973) A biaxial-tension creep-rupture testing machine. *J Strain Anal* 8(2):119–123
4. Dyson BF, Mclean D (1977) Creep of nimonic 80A in torsion and tension. *Metal Sci* 11(2):37–45. <https://doi.org/10.1179/msc.1977.11.2.37>

5. Stanzl S, Argon A, Tschegg E (1983) Diffusive intergranular cavity growth in creep in tension and torsion. *Acta Metall* 31(6):833–843
6. Kennedy C, Harms W, Douglas D (1959) Multiaxial creep studies on inconel at 1500 F. *J Basic Eng* 81(4):599–607
7. Chubb EJ, Bolton CJ (1980) Stress state dependence of creep deformation and fracture in AISI type 316 stainless steel. Mechanical Engineering Publications Limited, United Kingdom
8. Hayhurst D, Felce I (1986) Creep rupture under tri-axial tension. *Eng Fract Mech* 25(5):645–664. [https://doi.org/10.1016/0013-7944\(86\)90030-5](https://doi.org/10.1016/0013-7944(86)90030-5)
9. Sakane M, Hosokawa T (2001) Biaxial and triaxial creep testing of type 304 stainless steel at 923 k. In: IUTAM symposium on creep in structures, Springer, pp 411–418
10. Larson FR, Miller J (1952) A time-temperature relationship for rupture and creep stresses. *Trans ASME* 74:765–775
11. Tresca HE (1864) Sur l'écoulement des corps solides soumis a de fortes pressions, Imprimerie de Gauthier-Villars successeur de Mallet-Bachelier, rue de Seine
12. Mises RV (1913) Mechanik der festen körper im plastisch-deformablen zustand. *Nachrichten von der Gesellschaft der Wissenschaften zu Göttingen, Mathematisch-Physikalische Klasse*, pp 582–592
13. Hayhurst D (1972) Creep rupture under multi-axial states of stress. *J Mech Phys Solids* 20(6):381–382. [https://doi.org/10.1016/0022-5096\(72\)90015-4](https://doi.org/10.1016/0022-5096(72)90015-4)
14. Leckie F, Hayhurst D (1974) Creep rupture of structures. *Proc R Soc Lond A Math Phys Sci* 340(1622):323–347
15. Leckie F, Hayhurst D (1977) Constitutive equations for creep rupture. *Acta Metall* 25(9):1059–1070
16. Hayhurst DR, Leckie FA, Morrison CJ (1978) Creep rupture of notched bars. *Proc R Soc A Math Phys Eng Sci* 360(1701):243–264. <https://doi.org/10.1098/rspa.1978.0066>
17. Huddleston R (1985) An improved multiaxial creep-rupture strength criterion. *J Press Vessel Technol* 107(4):421–429
18. Huddleston R (1993) Assessment of an improved multiaxial strength theory based on creep-rupture data for type 316 stainless steel. *J Press Vessel Technol* 115(2):177–184
19. Huddleston R (1993) Assessment of an improved multiaxial strength theory based on creep-rupture data for Inconel 600. *Tech. Rep.*, Oak Ridge National Laboratory (ORNL), Oak Ridge, TN. <https://doi.org/10.2172/10168640>
20. American Society of Mechanical Engineers (2019) ASME Boiler and Pressure Vessel Code Section III, Division 5. American Society of Mechanical Engineers
21. American Society of Mechanical Engineers and American Petroleum Institute (2016) Fitness-For-Service, API 579–1/ASME FFS-1. American Society of Mechanical Engineers and American Petroleum Institute
22. EDF Energy Nuclear Generation Ltd (2012) Assessment Procedure for the High Temperature Response of Structures, R5. British. Energy
23. AFCEN (2015) RCC-MRx, AFCEN
24. Nassif O, Truster TJ, Ma R, Cochran KB, Parks DM, Messner MC, Sham T-L (2019) Combined crystal plasticity and grain boundary modeling of creep in ferritic-martensitic steels: I. Theory and implementation. *Modell Simul Mater Sci Eng* 27(7):075009. <https://doi.org/10.1088/1361-651X/ab359c>
25. Kloc L, Sklenička V (1997) Transition from power-law to viscous creep behaviour of p-91 type heat-resistant steel. *Mater Sci Eng A* 234:962–965
26. Haney EM, Dalle F, Sauzay M, Vincent L, Tournié I, Allais L, Fournier B (2009) Macroscopic results of long-term creep on a modified 9Cr–1Mo steel. *Mater Sci Eng A* 510:99–103
27. Sham T-L, Needleman A (1983) Effects of triaxial stressing on creep cavitation of grain boundaries. *Acta Metall* 31(6):919–926. [https://doi.org/10.1016/0001-6160\(83\)90120-7](https://doi.org/10.1016/0001-6160(83)90120-7)
28. Needleman A, Rice JR (1980) Plastic creep flow effects in the diffusive cavitation of grain boundaries. *Acta Metall* 28(10):1315–1332. [https://doi.org/10.1016/0001-6160\(80\)90001-2](https://doi.org/10.1016/0001-6160(80)90001-2)
29. Van Der Giessen E, der Burg MWD, Needleman A, Tvergaard V (1995) Void growth due to creep and grain boundary diffusion at high triaxialities. *J Mech Phys Solids* 43(1):123–165. [https://doi.org/10.1016/0022-5096\(94\)00059-E](https://doi.org/10.1016/0022-5096(94)00059-E)
30. Van Der Giessen E, Tvergaard V (1996) Micromechanics of intergranular creep failure under cyclic loading. *Acta Mater* 44(7):2697–2710
31. Onck P, Van Der Giessen E (1998) Growth of an initially sharp crack by grain boundary cavitation. *J Mech Phys Solids* 47(1):99–139. [https://doi.org/10.1016/S0022-5096\(98\)00078-7](https://doi.org/10.1016/S0022-5096(98)00078-7)
32. Raj R, Ashby M (1971) On grain boundary sliding and diffusional creep. *Metall Trans* 2(4):1113–1127
33. Ashby M (1972) Boundary defects, and atomistic aspects of boundary sliding and diffusional creep. *Surf Sci* 31:498–542
34. Crossman F, Ashby M (1975) The non-uniform flow of polycrystals by grain-boundary sliding accommodated by power-law creep. *Acta Metall* 23(4):425–440
35. Quey R, Dawson P, Barbe F (2011) Large-scale 3d random polycrystals for the finite element method: generation, meshing and remeshing. *Comput Methods Appl Mech Eng* 200(17–20):1729–1745
36. Manjoine MJ (1975) Ductility indices at elevated temperature. *J Eng Mater Technol* 97(2):156–161. <https://doi.org/10.1115/1.3443276>
37. Cocks A, Ashby M (1982) On creep fracture by void growth. *Prog Mater Sci* 27(3–4):189–244
38. Spindler M (2007) An improved method for calculation of creep damage during creep–fatigue cycling. *Mater Sci Technol* 23(12):1461–1470
39. Yatomi M, Nikbin K (2014) Numerical prediction of creep crack growth in different geometries using simplified multiaxial void growth model. *Mater High Temp* 31(2):141–147
40. le Graverend J-B, Adrien J, Cormier J (2017) Ex-situ X-ray tomography characterization of porosity during high-temperature creep in a Ni-based single-crystal superalloy: toward understanding what is damage. *Mater Sci Eng A* 695:367–378
41. Andrea R (2021) Data for article accurate effective stress measures: predicting creep life for 3d stresses using 2d and 1d creep rupture simulations and data. <https://doi.org/10.17632/kcbcnwyygr.1>, Mendeley Data, V1
42. Kimura K, Kushima H, Sawada K (2009) Long-term creep deformation property of modified 9Cr–1Mo steel. *Mater Sci Eng A* 510–511(C):58–63. <https://doi.org/10.1016/j.msea.2008.04.095>
43. Kimura K, Sawada K, Kushima H (2010) Creep rupture ductility of creep strength enhanced ferritic steels, American Society of Mechanical Engineers. *Press Vessels Pip Div* 6:837–846. <https://doi.org/10.1115/PVP2010-25297>
44. Jones E, Oliphant T, Peterson P et al (2001) SciPy: open source scientific tools for Python. <http://www.scipy.org/>
45. Byrd RH, Gilbert JC, Nocedal J (2000) A trust region method based on interior point techniques for nonlinear programming. *Math Program* 89(1):149–185
46. Abe F (2016) Heat-to-heat variation in creep life and fundamental creep rupture strength of 18Cr–8Ni, 18Cr–12Ni–mo, 18Cr–10Ni–Ti, and 18Cr–12Ni–Nb stainless steels. *Metall Mater Trans A* 47(9):4437–4454

47. Henry BS, Luxmoore AR (1997) The stress triaxiality constraint and the Q-value as a ductile fracture parameter. *Eng Fract Mech* 57(4):375–390. [https://doi.org/10.1016/s0013-7944\(97\)00031-3](https://doi.org/10.1016/s0013-7944(97)00031-3)
48. Messner MC, Nassif O, Ma R, Truster TJ, Cochran K, Parks D, Sham T-L (2019) Combined crystal plasticity and grain boundary modeling of creep in ferritic-martensitic steels: II. The effect of stress and temperature on engineering and microstructural properties. *Modell Simul Mater Sci Eng* 27(7):075010. <https://doi.org/10.1088/1361-651X/ab359f>
49. Nicolas A, Messner MC, Sham T-L (2021) A method for predicting failure statistics for steady state elevated temperature structural components. *Int J Press Vessels Pip* 192:104363